Winter ocean-ice interactions under thin sea ice observed by IAOOS platforms during N-ICE2015: Salty surface mixed layer and active basal melt

Zoé Koenig, Christine Provost, Nicolas Villacieros Robineau, Nathalie Sennéchael, Amelie Meyer

AGU PUBLICATIONS

JGR

Journal of Geophysical Research: Oceans

RESEARCH ARTICLE

10.1002/2016JC012195

Special Section:
Atmosphere-ice-ocean-ecosystem Processes in a Thinner Arctic Sea Ice Regime: The Norwegian Young Sea ICE Cruise 2015 (N-ICE2015)

Winter ocean-ice interactions under thin sea ice observed by IAOOS platforms during N-ICE2015: Salty surface mixed layer and active basal melt

Zoé Koenig[1], Christine Provost[1], Nicolas Villacieros-Robineau[1], Nathalie Sennéchael[1], and Amelie Meyer[2]

[1]Laboratoire LOCEAN-IPSL, Sorbonne Universités, UPMC, Univ. Paris 6, CNRS-IRD-MNHN, Paris, France, [2]Norwegian Polar Institute, Fram Centre, Tromsø, Norway

Key Points:
- Large sea-ice melt over the inflowing Atlantic Water on the Svalbard northern continental slope in winter
- Sea-ice bottom melt associated with near-inertial waves and tides
- Winter hydrography shows a salty mixed layer and three Atlantic Water pathways across and around the Yermak Plateau

Correspondence to:
Z. Koenig,
zklod@locean-ipsl.upmc.fr

Citation:
Koenig, Z., C. Provost, N. Villacieros-Robineau, N. Sennéchael, and A. Meyer (2016), Winter ocean-ice interactions under thin sea ice observed by IAOOS platforms during N-ICE2015: Salty surface mixed layer and active basal melt, *J. Geophys. Res. Oceans*, *121*, 7898–7916, doi:10.1002/2016JC012195.

Received 28 JUL 2016
Accepted 1 OCT 2016
Accepted article online 5 OCT 2016
Published online 28 OCT 2016

Abstract IAOOS (Ice Atmosphere Arctic Ocean Observing System) platforms, measuring physical parameters at the atmosphere-snow-ice-ocean interface deployed as part of the N-ICE2015 campaign, provide new insights on winter conditions North of Svalbard. The three regions crossed during the drifts, the Nansen Basin, the Sofia Deep, and the Svalbard northern continental slope featured distinct hydrographic properties and ice-ocean exchanges. In the Nansen Basin, the quiescent warm layer was capped by a stepped halocline (60 and 110 m) and a deep thermocline (110 m). Ice was forming and the winter mixed layer salinity was larger by ~0.1 g/kg than previously observed. Over the Svalbard continental slope, the Atlantic Water (AW) was very shallow (20 m from the surface) and extended offshore from the 500 m isobath by a distance of about 70 km, sank along the slope (40 m from the surface) and probably shed eddies into the Sofia Deep. In the Sofia Deep, relatively warm waters of Atlantic origin extended from 90 m downward. Resulting from different pathways, these waters had a wide range of hydrographic characteristics. Sea-ice melt was widespread over the Svalbard continental slope and ocean-to-ice heat fluxes reached values of 400 W m^{-2} (mean of ~150 W m^{-2} over the continental slope). Sea-ice melt events were associated with near 12 h fluctuations in the mixed-layer temperature and salinity corresponding to the periodicity of tides and near-inertial waves potentially generated by winter storms, large barotropic tides over steep topography, and/or geostrophic adjustments.

1. Introduction

With the rapid sea-ice decline [*Comiso*, 2012], the Arctic is the region in the world where climate change is most evident. The Arctic Ocean carries a large amount of ocean heat that has to be taken into account in the energy balance at the ice-ocean-atmosphere interface. Atlantic Water (AW) entering the Arctic Ocean through the Fram Strait with the West Spitsbergen Current (WSC) provides the main source of heat and salt to the Arctic Basin [*Schauer et al.*, 2008; *Aagaard et al.*, 1987]. The WSC splits into three branches upstream from the Yermak Plateau (Figure 1) [*Quadfasel et al.*, 1987; *Manley et al.*, 1992]: one branch recirculates back into the Fram Strait between 78°N and 80°N [*Hattermann et al.*, 2016]; a narrow branch follows the western slope of the Yermak Plateau along the 1000 m isobath (called hereafter the Yermak Branch, YB) [*Manley et al.*, 1992; *Manley*, 1995] and a main branch follows the northern continental slope of the Svalbard Archipelago along the 400–500 m isobath (called hereafter the Svalbard Branch, SB) [*Sirevaag et al.*, 2011; *Muench et al.*, 1992; *Cokelet et al.*, 2008]. The Yermak Branch and the Svalbard Branch recombine east of the Yermak Plateau to continue as a boundary current eastward along the Eurasian continental slope [*Rudels et al.*, 2015].

A cold and fresh mixed layer lies above a strong pynocline and usually prevents the upwelling of AW up to the surface and hence sea-ice melt. This upper layer originates from low salinity shelf waters in most of the deep basins except in the Nansen Basin [*Rudels*, 2016]. In the Nansen Basin, as the warm AW inflow encounters and melts sea ice, it creates an upper, low salinity surface layer that isolates the warm water from the sea ice and the atmosphere. The mixed layer in the Nansen Basin northeast of Svalbard forms as a result of AW cooling and freshening from sea-ice melt in the upper part of the water column. The AW heat released in the process is partly consumed by ice melt and partly escapes to the atmosphere. Evidence of basal sea-ice melt has been observed northeast of Svalbard in autumn [*Steele and Morison*, 1993] and on the Yermak

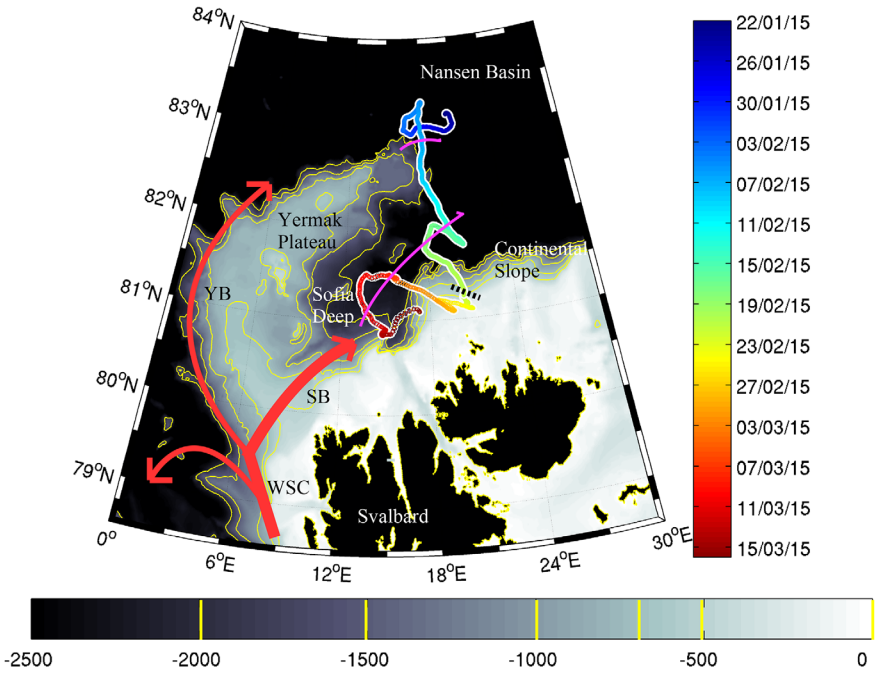

Figure 1. Drift trajectory of the IAOOS platform during Floe 1 of N-ICE2015 campaign. Vertical colorbar is time. The Atlantic Water inflow of the West Spitsbergen Current (WSC) splits into three branches, a recirculation to Fram Strait, the Yermak Branch (YB), and the Svalbard Branch (SB) [*Sirevaag et al*., 2011]. The dashed line indicates the location of Floe 1 breakup when R/V Lance left and IAOOS7 continued drifting alone. The two magenta lines show the offshore limit of the water originating from the Svalbard Branch over the Svalbard continental slope and the boundary between the Nansen Basin hydrography and the Sofia Deep hydrography, according to the data. Background is bathymetry (m). Yellow isolines are 0, 500, 700, 1000, 1500, and 2000 m. Bathymetry is from IBCAO (http://www.ngdc.noaa.gov/mgg/bathymetry/arctic/arctic.html).

Plateau from late January to Mid-March 2003 [*Mc Phee et al*., 2003]. Winter sea-ice melt is also documented by ice mass balance instrument during winter 2015 over the Svalbard Continental slope with ocean-to-ice heat fluxes peaking at 400 W m^{-2} (C. Provost et al., Observations of snow-ice formation in a thinner Arctic sea ice regime during the N-ICE2015 campaign: Influence of basal ice melt and storms, submitted to *Journal of Geophysical Research*, 2016). The trend in winter ice area loss North of Svalbard is close to 10% per decade and the ice edge has retreated to the northeast along the AW pathway [*Onarheim et al*., 2014; *Ivanov et al*., 2012]. *Ivanov et al*. [2016] suggest that the reemerging anomalies of ice free areas in midwinter Northeast of Svalbard reveal a positive feedback with a "memory" of ice depleted conditions in summer transferring to mid-winter via thinner ice more susceptible to lead formation allowing convection-induced upward heat fluxes from the AW.

The Norwegian young sea ICE (N-ICE2015) expedition from January to June 2015 took place in this region north of Svalbard to study ice-ocean-atmosphere interactions in a thinner Arctic sea-ice regime than it used to be (Figure 1). This 6 month long campaign consisted of four drifting ice camps, relocated northward each time the floes broke [*Granskog et al*., 2016]. The general hydrography and circulation patterns observed during the 6-month drift are presented in Meyer et al. (A. Meyer et al., Winter to summer hydrographic and current observations in the Arctic north of Svalbard, submitted to *Journal of Geophysical Research*, 2016). Here we focus on mid-winter conditions as documented by IAOOS (Ice Atmosphere Arctic Ocean Observing System) platforms deployed during Floe 1 of N-ICE2015 in January–February 2015 in the middle of the polar night. These platforms carry an ice mass balance instrument monitoring temperature across the air/snow/ice/ocean interface and an ocean profiler measuring conductivity hence salinity, temperature and dissolved oxygen concentration down to 500 m or more. We use the IAOOS platform data to examine the winter hydrography in the region and the ocean processes responsible for the winter basal sea-ice melt over the Svalbard continental slope.

Section 2 presents the IAOOS platforms, the data processing and the platform drift over the western Nansen Basin, the Sofia Deep and the Svalbard northern continental slope (Figure 1). Section 3 describes the distinct

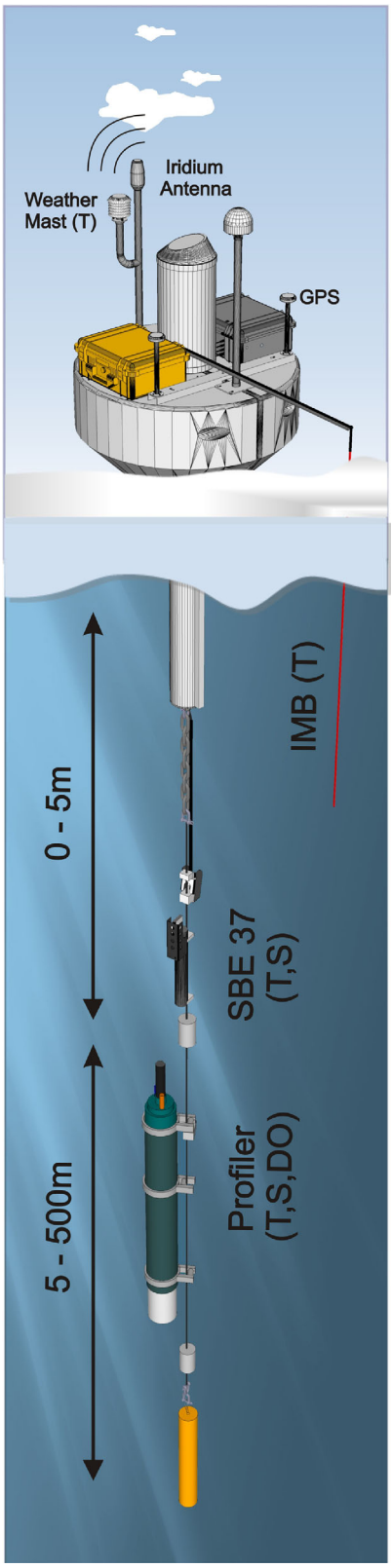

Figure 2. Schematic of the IAOOS platform showing weather mast, GPS, data transmission unit, ice mass balance unit (IMB measuring temperature through air, snow, ice, and upper ocean), SBE37 instrument (recording temperature and salinity at 4 m depth) and the ocean profiler (measuring temperature, salinity, and dissolved oxygen concentration from 5 to 500 m depth).

hydrographic conditions sampled by the profilers in the three regions. Section 4 focuses on the ocean-ice interface with sea-ice growth and basal melt processes. Finally in section 5 results are discussed and conclusions are drawn out.

2. IAOOS Platform and Data

The IAOOS autonomous platforms (Figure 2) document the four media, ocean/ice/snow/atmosphere, in the Arctic while drifting with the ice [*Provost et al.*, 2015]. The atmospheric part includes a GPS, a weather mast and a microlidar [*Mariage*, 2015; *Mariage et al.*, 2016]; the ice/snow part an ice mass balance instrument [*Jackson et al.*, 2013]; and the ocean part an ice-tethered profiler [*Provost et al.*, 2015] (Figure 2). Other ice-tethered CTD profiling systems are used in the Arctic [e.g., *Krishfield et al.*, 2008; *Kikuchi et al.*, 2007]. Two platforms were deployed during Floe 1 (IAOOS7 on 22 January and IAOOS8 on 26 January, Table 1). Additional profiler tests (IAOOS 9) were carried out from 6 February to 19 February from a tent-covered testing hole on Floe 1. The three platforms were initially located close to the ship, less than 500 m from each other on a second year ice floe, Floe 1. R/V Lance drifted with Floe 1 from 15 January 15 (83.22°N, 21.26°E) until 21 February (81.22°N, 20.34°E) when the floe broke up (Figure 1). IAOOS 8 and 9 platforms were recovered during Floe 1 breakup while IAOOS 7 platform pursued its drift until its recovery by R/V Lance on March 16 (Figure 1). The profiler on IAOOS 7 was lost on 21 February as the

Table 1. Characteristics of the IAOOS Platforms

	IAOOS 7	IAOOS 8	IAOOS 9
Deployment date	22 Jan 2015	26 Jan 2015	06 Feb 2015
Profiler lost	21 Feb 2015	21 Feb 2015	
Recovery date	26 Mar 2015	23 Feb 2015	19 Feb 2015
Sampling rate (h)	12	12	12
Wire Length (m)	500	500	850
SBE37	No	Yes	No
IMB	Yes	Yes	No
Good Profiles *T*	62	50	26
Good Profiles *S*	53	47	25
Good Profiles DO	47	44	21

platforms drifted over ocean depths smaller than 500 m (Table 1). Thus, from that date on, the only ocean data available are the near-ice ocean temperature profiles from the ice mass balance instrument.

The IAOOS weather mast provides local atmospheric conditions. The ocean data collected from the IAOOS platforms document the warm water layer from the Atlantic Water inflow, the halocline, the mixed layer, the ocean-to-ice heat flux and consequent winter basal ice melt (mid-January to mid-March 2015). The snow/ice mass balance instrument data is analyzed in detail by Provost et al. (submitted manuscript) with a focus on snow-ice formation observed in February and March 2015. Here we use the ice instrument data to examine closer the ocean-ice interface.

The IAOOS weather mast recorded cold air temperatures below −30°C until 1 February and signatures of the six main storms identified during N-ICE2015 by *Hudson and Cohen* [2015]: M1 (21–22 January), M2 (3–8 February), M3 (15–21 February), M4 (3–4 March), M5 (8–10 March), and M6 (15–16 March) with air temperature increase (up to 0°C on 17 February) and large decrease in sea level pressure (down to 960 hPa on 9 March) (Figure 3a). M4 and M5 are recorded after Floe 1 breakup and the ship was not close to the IAOOS platforms anymore. Hence, dates of M4 and M5 have been adjusted from *Hudson and Cohen* [2015] using the data from the IAOOS weather mast. The GPS-derived platform drift speed increased during the storms and reached 40 cm s^{-1} during M2, 60 cm s^{-1} on 16 February (M3), and even 100 cm s^{-1} during M6 (Figure 3b).

The ice mass balance instrument from the Scottish Association for Marine Sciences (SAMS), hereafter called SIMBA standing for SAMS ice mass balance for the Arctic, is composed of a thermistor chain of 5 m that provides profiles of temperature and a proxy of the thermal resistivity of the media with a 2 cm vertical resolution [*Jackson et al*., 2013]. The accuracy of each temperature sensor is 0.1°C. SIMBA data from IAOOS 7 and 8 (SIMBA_2015h and SIMBA_2015i, respectively) have a 3 h sampling frequency. The SIMBA data analysis that identifies the air/snow, snow/ice, and ice/ocean interfaces and estimates of heat flux densities is detailed in Provost et al. (submitted manuscript). Here we use temperature data from SIMBA_2015h which is the longest record with 51 days from 24 January to 16 March (Figure 3c). Snow thickness was 55 cm at deployment and increased to 90 cm during storm M3 (Figure 3c). Ice thickness was 154 cm at deployment, decreased to 125 cm on 9 March due to basal melt, and then increased to 145 cm from 9–11 March due to snow-ice formation (Provost et al. submitted manuscript). The temperature time derivative (Figure 3d) shows high-frequency variations in the atmosphere until storm M3 (there are no more sensors in the atmosphere after M3 storm snow fall) that are dampened in the snow. In the ice the major changes in temperature are the cooling due to the initial refreezing of the deployment hole (until 1 February) and the exothermal formation of snow-ice on 9 March. Changes in ocean temperature resulted in basal ice melt that starts on 16 February.

The ocean profilers, from French manufacturer NKE (PROVOR SPI), a sliding profiler with inductive transmission, carried a Seabird SBE41CP CTD (Conductivity, Temperature, Depth) with an Aanderaa 4330 dissolved oxygen (DO) optode. The profilers were set to perform two profiles a day from 500 m upward (850 m for IAOOS9) starting at 6 am and 6 pm. They gathered a total of 138 profiles (62, 50, and 26 profiles for IAOOS7, IAOOS8, and IAOOS 9, respectively; Table 1). The vertical resolution of the processed CTD data is 1 dbar in the upper 400 dbars, 5 dbars from 400 to 550 dbars, and 10 dbars from 550 to 850 dbars; the vertical resolution in DO is 2 dbars over all depths. Salinity was calibrated and quality controlled using the ship CTD salinity bottles (four dates) (Meyer et al., submitted manuscript). Following quality control, we retain all the temperature profiles and remove 1% of the salinity profiles. Finally, the accuracy is estimated to be 0.002°C in temperature, and 0.02 g/kg in salinity. Several profiles are missing or incomplete because of high drift speeds (>0.4 m s^{-1}) impeding the ascent of the profiler. There were no bottle DO measurements available during Floe 1 of N-ICE2015 to calibrate the DO data. DO accuracy is estimated comparing the deep values

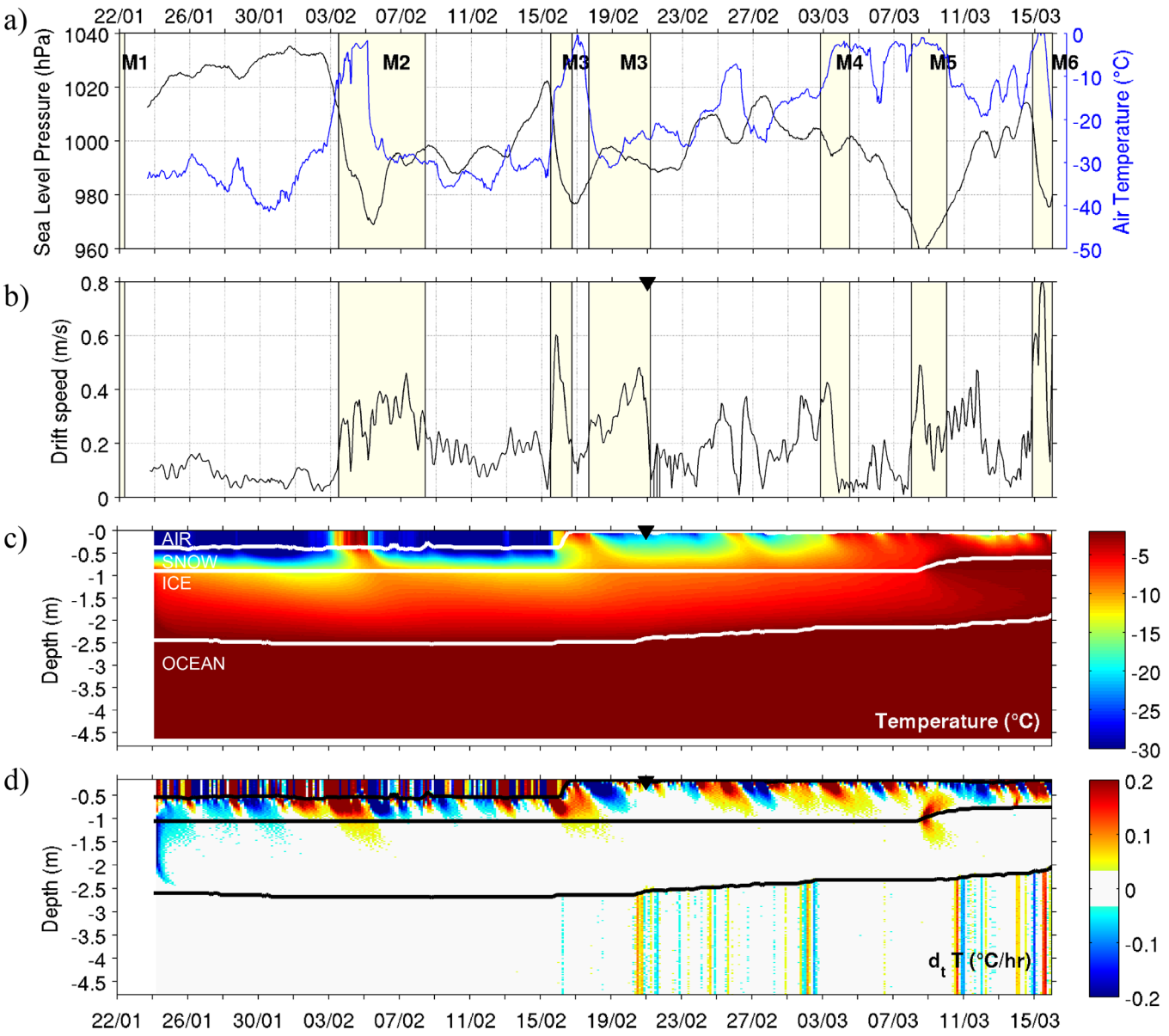

Figure 3. Atmospheric and SIMBA data from 22 January to 16 March: (a) Sea level pressure and air temperature. Major storms are shaded in light yellow (M1, M2, . . .). (b) Drift velocity estimated from GPS positions. (c) Temperature profiles from SIMBA (in °C), white lines from *Provost et al.* [2016] indicate the air/snow/ice/ocean interfaces. (d) Time derivative of the SIMBA temperatures (in °C/d). The black triangle indicates the date after which there are no profiler data.

of DO concentration (rather stable at 500m) between the three profilers. A difference of 3 μmol L^{-1} is observed between IAOOS 8 and 9, and IAOOS 7. An offset of 3 μmol L^{-1} is then applied to the oxygen data from IAOOS7 and the accuracy of the data is estimated to be at 3 μmol L^{-1}.

IAOOS 8 also featured a Seabird SBE37 CTD recorder at about 4 m depth, sampling temperature, salinity, and pressure every 5 min from 22 January to 21 February. However, freezing of the SBE37 during deployment prevents use of the temperature data before 27 January and of the salinity data before 6 February. The precision of the temperature sensor is 0.002°C and the conductivity sensor is 0.002 g/kg once converted in absolute salinity.

In summary, the ocean data consist of temperature profiles in the upper 2 m with a 3 h time resolution from SIMBA-2015h (record length 51 days), temperature and salinity at 4 m depth with a 5 min resolution from the SBE37 (record length 25 days for temperature and 15 days for salinity), and temperature, salinity, and DO concentration with a 12 h resolution from 5 to 500 m from the profiler (record length 30 days). The

horizontal resolution depends upon drift velocity: for the profiler data it varies from 2 km on 2 February to 23 km on 15 February with an average of about 10 km.

3. Hydrography North of Svalbard in January–February 2015

The hydrographic sections presented in Figure 4 are composites of the three ocean profiler data. We use the International Thermodynamic Equations of Seawater (TEOS-10) framework [*McDougall et al*., 2012] with conservative temperature CT (°C) and absolute salinity S_A (g/kg). In the region, absolute salinity values exceed practical salinity values by about 0.16. We follow water mass definitions from *Rudels et al*. [2000, Figure 2] (Figure 5a) adapted to absolute salinity and conservative temperature. The warm layer comprises two main water types: Modified Atlantic Water (MAW) (temperatures between 0 and 2°C) and Atlantic Water (AW) (temperatures larger than 2°C). DO concentration varies from low values (290–310 μmol L^{-1}) in the warm layer to larger values in the upper layer (range 340–367 μmol L^{-1}) (Figure 4c). The surface layer shows absolute salinities between 34.35 and 34.55 g/kg, corresponding to practical salinities of ∼34.19 and 34.39 psu, respectively, slightly larger than those observed previously in the region (e.g., 34.1–34.2 psu) [*Kikuchi et al*., 2004; *Rudels et al*., 2000; *Sirevaag and Fer*, 2009]. Near-surface temperatures are often at the freezing point or close to it. The three regions crossed by Floe 1 drift, the Nansen Basin from 22 January to 6 February, the Sofia Deep and the tip of the Yermak Plateau from 6 to 12 February and on 17 February (called hereafter Sofia Deep) and the Svalbard continental slope the rest of the time, present clearly distinct characteristics in the warm water layer and in the surface layer (Figures 1 and 4).

3.1. The Warm Water Layer From the Atlantic Ocean

The warm water layer (with temperatures larger than 0°C) extends from around 100 m to deeper than 500 m (Figure 4a), the deep 0°C isotherm is at about 800 m in the 850 m deep IAOOS 9 profiles (Figures 6a and 7a).

In the Nansen Basin (depth $>$ 4000 m), the warm water, composed of MAW, shows layering with two cores (at depths of around 250 and 400 m) with the same temperatures (around $+1.8$°C), different salinities (35.08 and 35.12 g/kg), and thus densities of 27.91 and 27.95, respectively (Figure 5a). The constant depth of the two cores is highlighted in the Brunt Väisälä frequency panel (Figure 4d). DO concentration is around 305 μmol L^{-1} in the MAW (Figures 4d and 5b). Hydrographic properties of Nansen Basin profiles (in blue in Figure 6) show little scatter in the AW range below 150 m. Isopycnals remain at the same depth except for significant isopycnal displacements at depth (80 m displacement at 400 m) after 3 February coincident with storm M2.

Over the continental slope off Svalbard, roughly from 12 February onward, the warm water is AW with a single shallower core (∼150 m), warmer temperature ($>$2.5°C), higher salinity ($>$35.15 g/kg), and slightly larger DO concentration (∼315 μmol L^{-1}) (Figure 5). This AW appears to come directly from Fram Strait (Figure 1) [*Sirevaag and Fer*, 2009]. The last profile (21 February) on the slope over 600 m shows AW as close as 20 m from the surface (black profile in Figures 5b and 6). It is the warmest profile below 300 m (2.9°C), and among the saltiest and the lowest in DO concentration (35.19 g/kg, 312 μmol L^{-1}). The peculiar upper structure of the profile is examined more closely in section 3.2. Profiles over the Svalbard Continental Slope show an offshore deepening of the top of the AW layer (0°C isotherm) and a scatter of hydrographic properties at depth indicative of lateral mixing. On 17 February, as the platform drifted to the north, the profiler sampled MAW from the Sofia Deep at 81.8°N and 18.5°E–19°E. This provides a local offshore limit of the location of the Atlantic Water coming from the Svalbard Branch (Figure 1, magenta line and Figure 7).

Between 6 and 12 February, the profiler measured water over the northern tip of the Yermak Plateau and over the Sofia Deep (Figures 1 and 4). The warm layer shows variations in isopycnal depths with amplitudes of about 100 m at 400 m decreasing toward the surface to values of 80 m at 200 m, and 10 m at 100 m. The troughs in isopycnal depth observed on 7 February likely correspond to topographically induced upwelling of deep fresher water that mixes with AW (Figure 7) (see section 5). Apart from these upwelling events, the warm layer comprises water from the Nansen Basin (Figure 4, 10–11 February). During 8 February and 11–12, the layer contains water warmer and saltier than in the Nansen Basin associated with isopycnal ridges. The warm water on 8 February at about 82.2°N located on the slope of the Yermak Plateau (depth around 1800 m) is probably the Yermak Branch, with an AW core at 300 m, propagating southward from the tip of

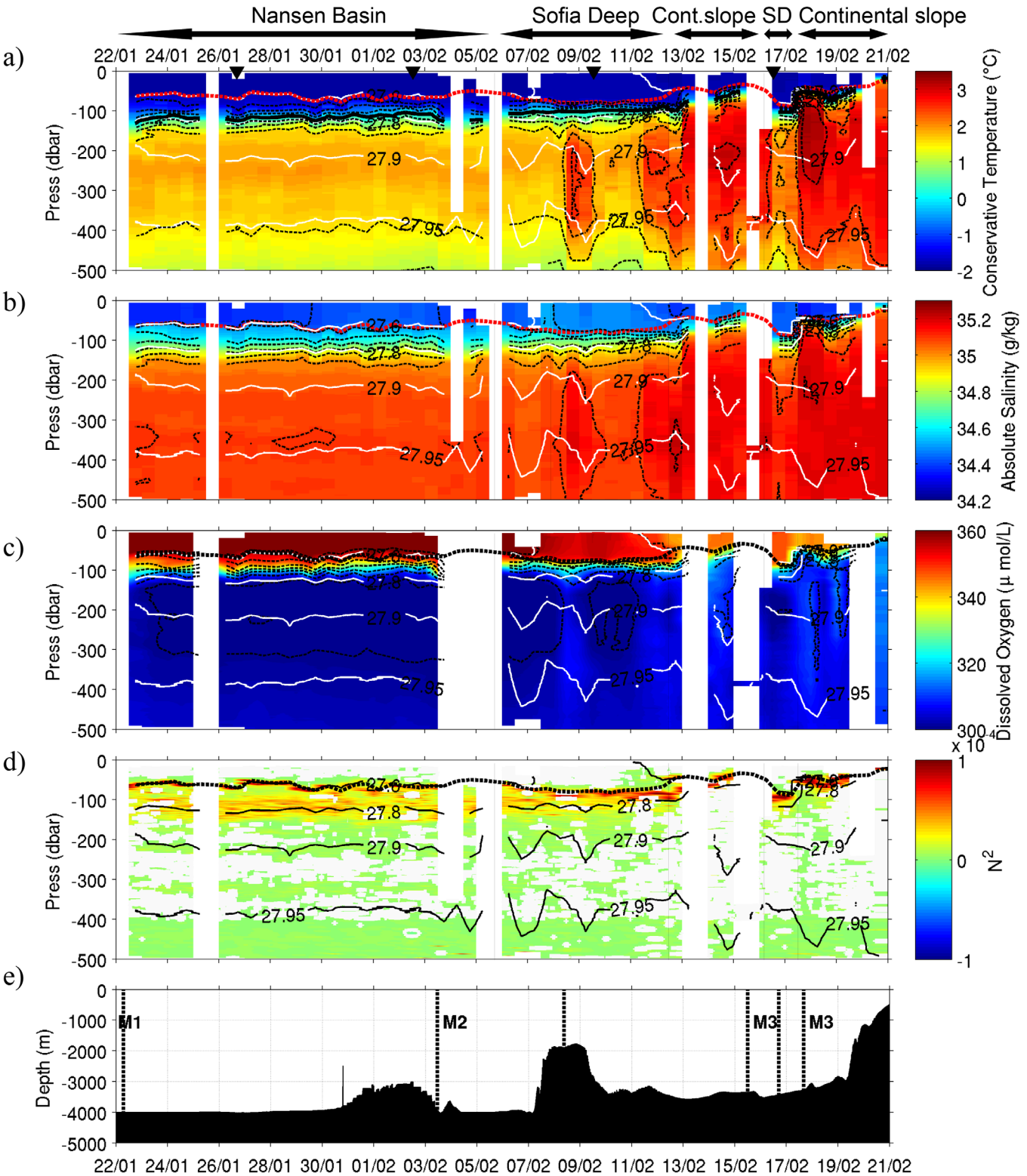

Figure 4. Composite section from the 3 profiler data (12 h averaged) of (a) conservative temperature (°C). The thick black line is the 0°C isotherm. (b) Absolute salinity (g/kg). (c) Dissolved oxygen concentration (μmol L^{-1}). Thin black dashed lines are, respectively, temperature, salinity, and dissolved oxygen concentration isolines. Thin white lines are isopycnals. (d) Brunt Väisälä frequency (N^2) along the drift (10^{-4} s^{-1}). The thin black lines are isopycnals. (e) Bathymetry along the drift trajectory. Dashed lines delimit storms. Thick dashed lines (red or black) are the mixed layer depth. Dates when the ship CTD were used to calibrate salinity data appear as black triangles. Arrows on the top indicate the "hydrographic regions" of Nansen Basin, Sofia Deep (SD), and Svalbard continental slope. Missing profiles are white.

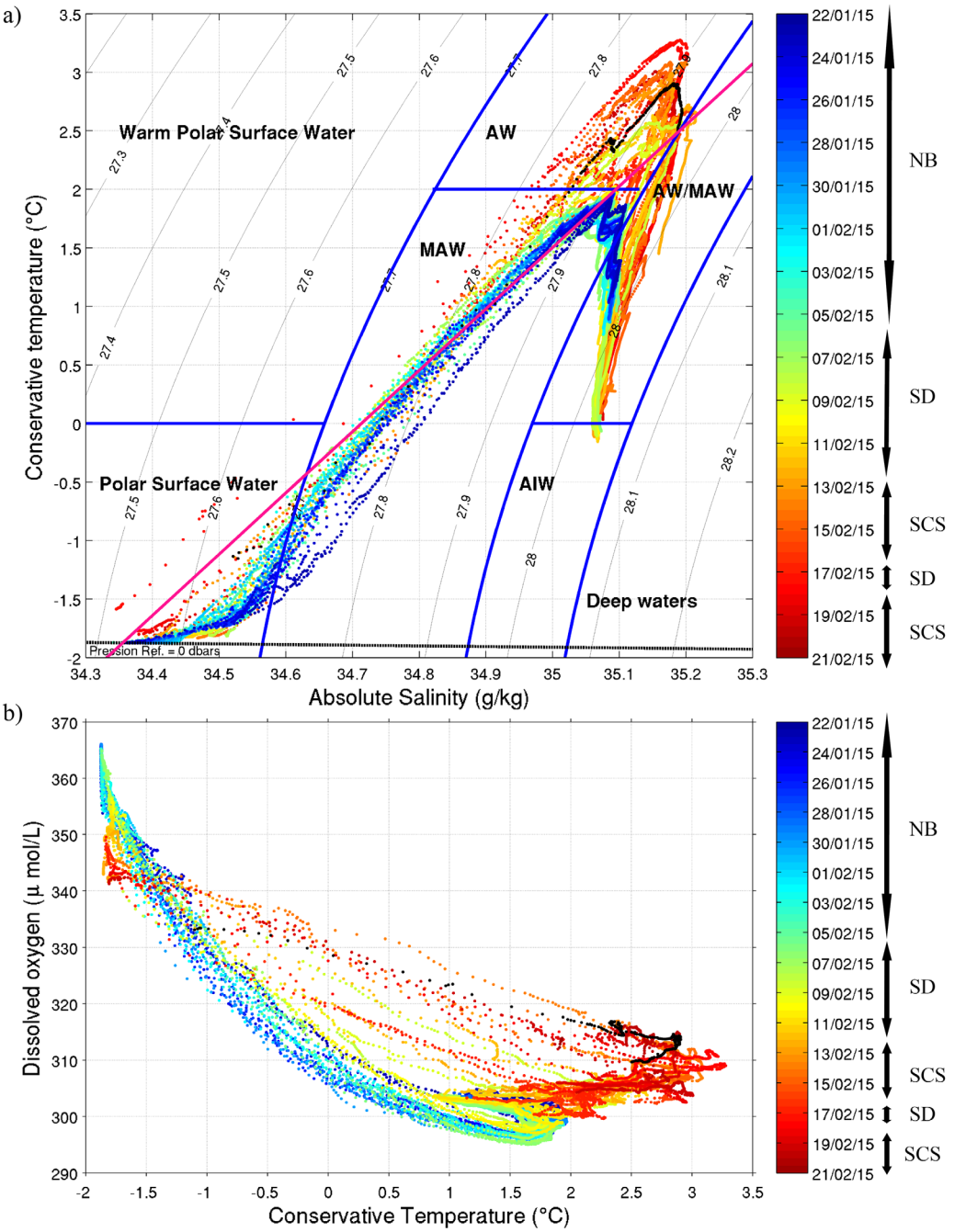

Figure 5. (a) Conservative temperature-absolute salinity diagram from the IAOOS profiler data. Water mass boundaries are from *Rudels et al.* [2000]: Atlantic Water (AW), Modified Atlantic Water (MAW), and Atlantic Intermediate Water (AIW). (b) Conservative temperature-DO concentration diagram. Colorbar is time and corresponding hydrographic provinces, Svalbard continental slope (SCS), Sofia Deep (SD), and Nansen Basin (NB), crossed during the drift are indicated. The black profile in both diagrams corresponds to the last one (20 February afternoon) over very shallow waters. The magenta line is the mixing line in the Nansen Basin between Polar Surface Water and Modified Atlantic Water. The blue dots under the magenta line in Figure 5a draw the shape of the convective halocline.

the Yermak Plateau (82.8°N, 16°E) following the 1000–2000 m isobath (Figures 1, 4, and 7). The warm water on 11–12 February (82.2°N, 19°E) with a core at 300 m may originate from a branch flowing through the Yermak Pass (a 700 m deep passage through the Yermak Plateau at 81°N) [*Gascard et al.*, 1995, Figure 34] or could be a deep eddy that detached from the Svalbard Branch and sank (Figure 7). There is not enough data to draw further conclusions. As a result of these different processes or paths, the range of hydrographic characteristics in the warm water layer is larger in the Sofia Deep profiles (red in Figure 6) than in the

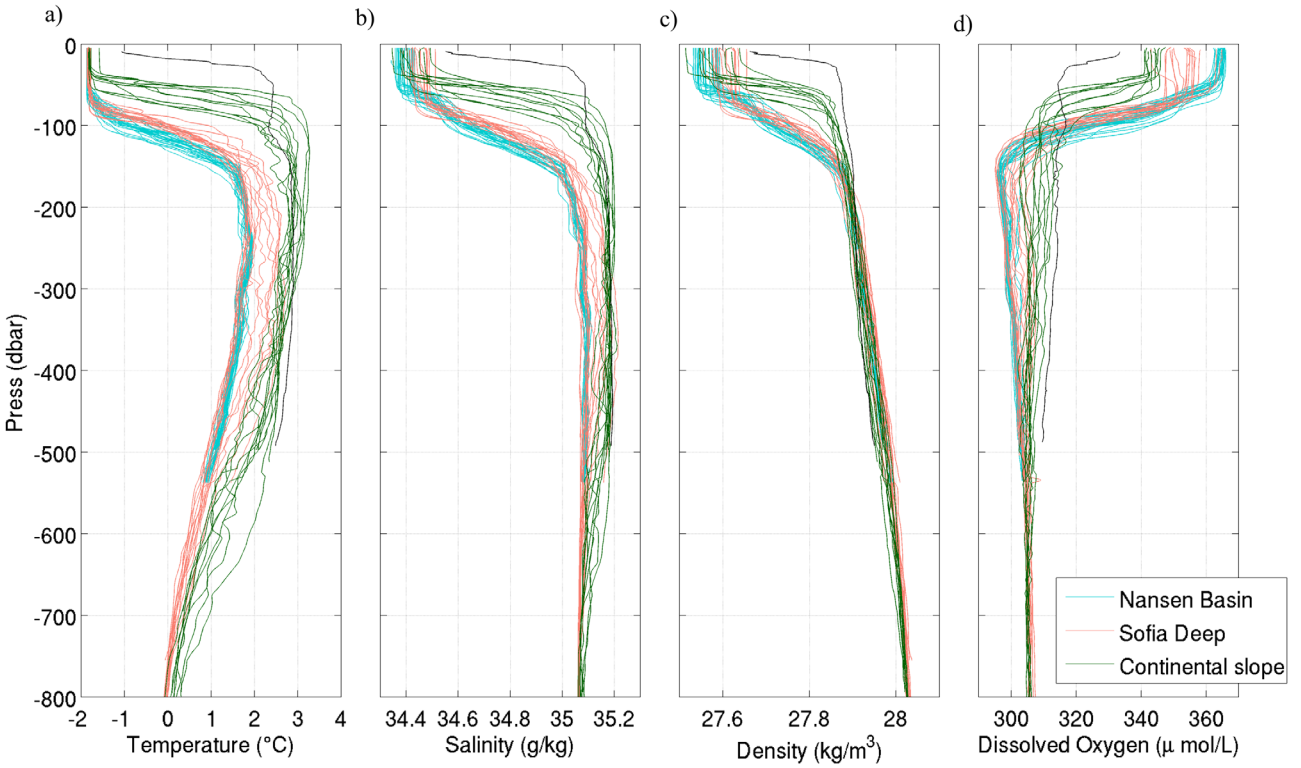

Figure 6. Vertical profiles from the profilers of (a) conservative temperature (°C), (b) absolute salinity (g/kg), (c) density (kg m^{-3}), and (d) dissolved oxygen concentration (μmol L^{-1}). Blue profiles are from the Nansen Basin, red profiles from the Sofia Deep and green profiles from the Svalbard continental slope. Black profiles correspond to the last profile of the drift (20 February afternoon) over very shallow waters.

Nansen Basin (blue in Figure 6) or the Svalbard continental slope profiles (green in Figure 6). In particular, the lowest salinity observed on 7 February where 35.05 g/kg at 300 m depth (Figure 6b), and the largest salinity at 370 m were 35.21 g/kg on 12 February (Figures 5a and 6b).

The AW is DO-enriched (from 300 to 315 μmol L^{-1}) compared to the MAW (295–305 μmol L^{-1}) indicating that warm waters from the Svalbard Branch have been in contact with the atmosphere more recently than waters from the Nansen Basin (Figures 4c and 5b). The Nansen Basin (MAW) profiles show a DO-minimum ($\sim$ 300 μmol L^{-1}) at about 140–150 m at the base of the lower halocline (blue in Figure 6d) whereas the shallowest Svalbard Branch (AW) profile (black in Figure 6d) is homogeneous below 20 m with DO values of 310 μmol L^{-1}. The spread in DO concentration in the other profiles is indicative of vertical mixing (Figure 6d).

3.2. The Upper Layer Characteristics

Over the Svalbard continental slope and the Sofia Deep, the depths of the thermocline, the halocline, and the pycnocline coincide. Gradients are steeper and shallower (40 m) above the Svalbard Branch, while weaker and deeper (90 m) over the Sofia Deep (Figure 6). Over the Nansen Basin, the thermocline is centered at 110 m whereas the halocline (pycnocline) comprises an upper halocline (upper pycnocline) centered at 60 m and a lower halocline (lower pycnocline) centered at 110 m (Figure 6). The processes responsible for this double pycnocline structure potentially involve formation of a convective cold halocline as ice is formed and/or the advection of cold salty water from shelves [e.g., *Rudels et al.*, 1996; *Kikuchi et al.*, 2004]. The observed T-S curves from the Nansen Basin fall below the mixing line joining T-S values at 220 and 140 m (magenta line in Figure 5) and form a bend separating low salinity freezing surface layers from the thermocline waters. Indeed, the lower halocline water and the top of the thermocline water have salinity larger (temperature lower) than the mixing line between the AW and the Polar Surface Water. This feature in the T-S diagram in the Nansen Basin indicates a convective mechanism leading to a stepped halocline after summer melt and refreezing [*Kikuchi et al.*, 2004, Figure 4].

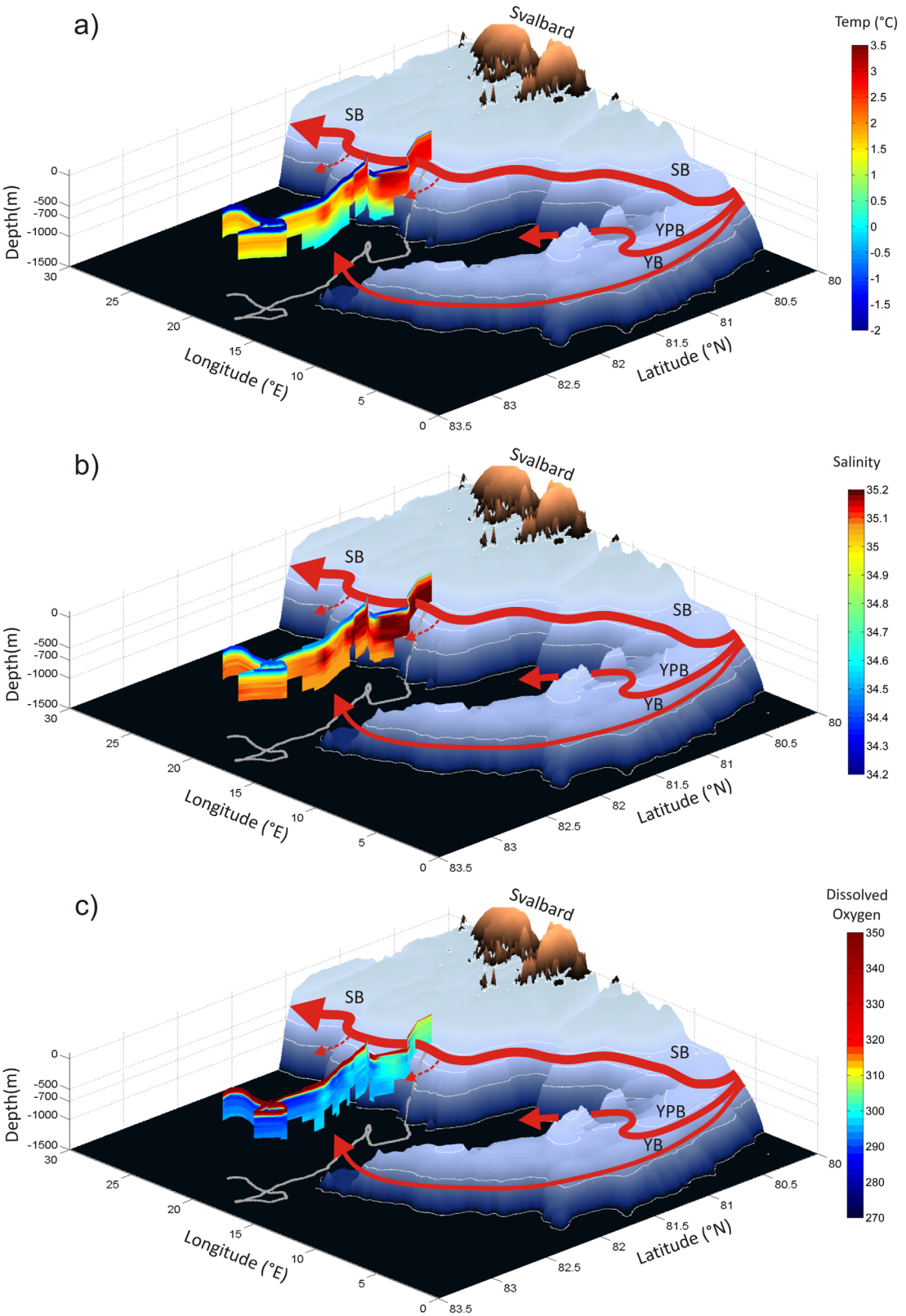

Figure 7. Three-dimensional plot of (a) conservative temperature (°C), (b) absolute salinity (g/kg), and (c) dissolved-oxygen concentration (μmol L^{-1}). Isolines are 500, 700, 1000, and 1500 m. Red full arrows describe paths for the warm Water Inflow: the Yermak Branch (YB), the Svalbard Branch (SB), and the Yermak Pass branch (YPB) [*Sirevaag et al.*, 2011; *Rudels et al.*, 2000]. Dashed red lines are indication of downwelling of the Atlantic Water down the continental slope into the Sofia Deep.

The last profile on the slope with near-surface Atlantic Water at 20 m measures the warmest and among the saltiest waters below 300 m and shows a stepped structure in both temperature and salinity, with a gradient at 130 m, compensated in density (black profile in Figures 5 and 6). Below 30 m depth, stratification is very weak (Figures 4d and 6c) and temperature and salinity profiles are well mixed on each side of the step (Figures 6a and 6b). This structure suggests the loss of heat in the upper 120 m laterally and vertically along the Svalbard Branch, followed by the advection of a layer of fresher melt water on top of it or active ice melt creating a sharp near-surface thermocline and halocline [*Rudels*, 2016].

Apart from this peculiar profile, on the slope, the mixed layer depth (MLD) (here defined as the depth where density is larger than the density at 10 m by 0.03 kg m^{-3}) is on average 40 m in the Svalbard Branch, 90 m in the Sofia deep, and 60 m in the Nansen Basin. Note that the MLD is quite insensitive to the precise criterion as the pycnocline is sharp [e.g., *Timmermans et al.*, 2012; *Toole et al.*, 2010]. The surface mixed layer is cold (∼−1.8°C, the freezing temperature), with low salinity (∼34.35–34.50 g/kg) and DO-enriched compared to the MAW/AW (∼340–370 μmol L^{-1}). The DO-enriched mixed layer corresponds to Polar Surface Water (Figure 5). The salinity range is quite large from 34.35 to 34.51 g/kg and even reaching 34.55 g/kg for the last profile (Figure 6b). These salinity values are high compared to MIMOC climatological values, +0.25 g/kg (Meyer et al., submitted manuscript).

The Brunt-Väisälä frequency [*Gill*, 1982] is larger above the Svalbard continental slope as the warm waters are denser in the AW than in the MAW (Figure 4d). The main pynocline reaches Brunt-Väisälä frequency values larger than 2×10^{-4} s^{-1} (Figure 4d), of the same order as in *Fer* [2009]. The deeper thermocline and lower halocline in the Nansen Basin show large Brunt-Väisälä frequency (5×10^{-5} s^{-1}) under the main pycnocline.

The mixed layer DO concentration is larger in the Nansen Basin than over the Svalbard Branch (360 μmol L^{-1} and 345 μmol L^{-1}, respectively, Figures 4c and 5b). This may be an indication of oxygen consumption and hence of biomass remineralization over the AW that does not occur in the mixed layer over the MAW. It may also be due to upwelling of low DO concentration AW through the pynocline over the Svalbard Branch that does not occur in the Nansen Basin.

4. Upper Ocean, Sea-Ice Formation and Basal Melt

We now focus on the ice-ocean interface in two steps, first analyzing and comparing the SIMBA, SBE37, and profiler data until 21 February, and then second by analyzing the only data available after 21 February which is the SIMBA temperature data.

4.1. Upper Ocean Until the Loss of the Profilers (21 February)

4.1.1. Consistency Between the Instruments in the Vertical

Temperature time series from the upper 2 m of the ocean from SIMBA (3 h resolution shown with an adapted colorbar to focus on the ice-ocean interface, Figure 8a) are consistent with the temperature time series at 4 m from the SBE37 (5 min sampling) (Figure 8e) and the temperature time series in the upper 30 m from the profiler (12 h sampling) (Figure 8b). Several events with under-ice temperatures above freezing temperature are identified.

The temperature increase observed from 7 to 11 February in the SIMBA, SBE37, and upper-ocean profiler data ($T \sim -1.75$°C; Figures 8a and 8b, Figure 8e) coincides with an increase in salinity measured by the SBE37 ($S \sim$ 34.35–34.5 g/kg) and the ocean profiler ($S \sim$ 34.48 g/kg; Figures 8e and 8c).

On 16, 18, and 20 February (Figure 8a), the under-ice temperature is above freezing (about 0.15°C, 0.2°C, and 1.8°C, respectively). The 18 and 20 February events are associated with warmer water down to the halocline (profiler data; $T \sim -1.55$°C and $T \sim -1$°C, respectively) (Figure 8b). There is no profiler data on 16 February. These three warm events occur over the Svalbard Branch, where the 0°C isotherm is shallow (between 60 and 18 m, Figure 8c).

From 30 January to 3 February, profiler data (below 8 m) indicate a salinity increase in the mixed layer (∼34.45 g/kg instead of ∼34.4 g/kg, Figure 8c), while temperature remains stable (around −1.85°C, Figure 8b). There is no signal in temperature in the upper 4 m of the ocean (SIMBA or SBE37) (Figures 8a and 8e). This salinity-only event happens before M2, when the platform is located on the edge of the slope of the

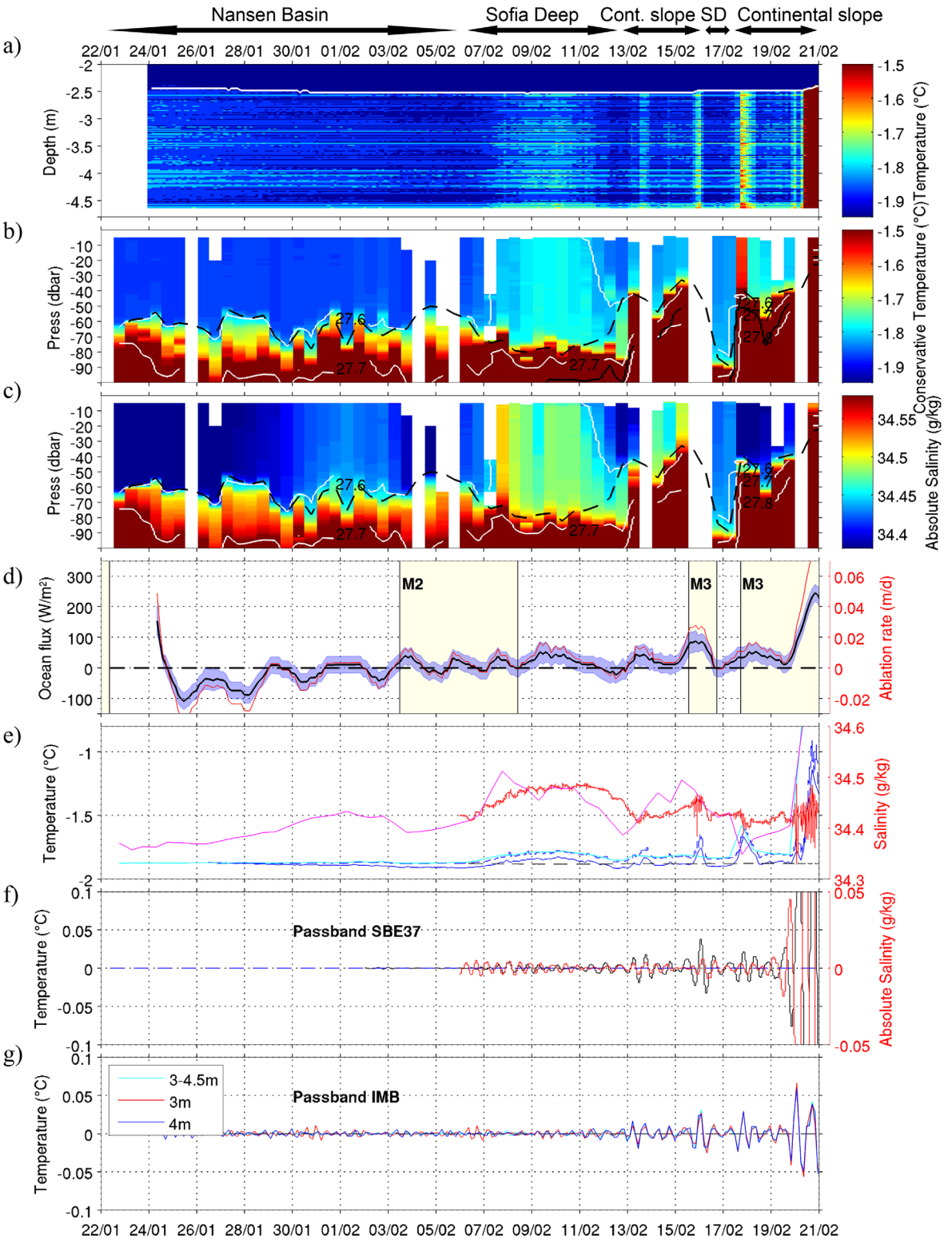

Figure 8. (a) SIMBA temperature zoomed on the ocean (scale −2°C; −1.5°C). (b) Conservative temperature (°C) in the upper 100 m from the profilers. The full black line is the 0°C isotherm. (c) Absolute salinity (g/kg) in the upper 100 m from the profilers. White lines are isopycnals. The thick dashed line is the mixed layer depth. Missing data points are white. (d) Ocean Flux (left axis, W m^{-2}) and ablation rate (right axis, m/d), at the ice/ocean interface deduced from SIMBA data [*Provost et al.*, 2016]. Blue shaded area is the ocean heat flux uncertainty [*Provost et al.*, 2016]. Storm periods are shaded in light yellow. (e) Left axis: temperature from SIMBA (mean of the upper 2 m, 3 h sampling, blue), from SBE37 (4 m, 5 min sampling, dashed blue) and from profilers at 20 m (12 h sampling, cyan). The dotted line is the freezing temperature. Right axis: Salinity from SBE37 (red) and from profilers at 20 m (magenta). (f) Data from SBE37 filtered between 8 and 16 h: temperature (left axis, black), salinity (right axis, red). (g) Band-pass filter between 8 and 16 h of SIMBA temperatures at 3 m (red), 4 m (blue), and averaged between 3 and 4.5 m (black).

Yermak Plateau (seafloor depth about 3000 m). A salty mixed layer is characteristic of the Yermak Plateau (Meyer et al., submitted manuscript).

The ocean (SIMBA, profilers and SBE37) data, therefore, provide a consistent picture of the upper-ocean vertical structure despite the difference in time resolution (3 h for the SIMBA, 12 h for the profiler and 5 min for the SBE37). For the following, it is important to recall that in the Nansen Basin the thermocline located at about 90 m depth is deeper than the pycnocline/halocline (around 60 m), while in the Sofia Deep and Svalbard Branch the three gradients coincide and are shallower than 60 m, around 40 m. The ocean heat flux (Figure 8d) was estimated as the sum of the latent heat flux (calculated from the time evolution of the ice-ocean interface depth) and the conductive flux in the ice next to the ocean interface (calculated from the vertical derivative of temperature) (Provost et al., submitted manuscript). The negative fluxes at the beginning of the time series until 26 January (Figure 3d) correspond to lateral fluxes associated with the refreezing of the deployment hole of the SIMBA. From 26 January to 1 February, sea-ice formation (growth) most likely caused the negative fluxes in accordance with the formation of the stepped halocline in the Nansen Basin. The ocean flux is significantly positive on several occasions, 9–11 February (50 W m^{-2}), 16 February (100 W m^{-2}), and 20 February (250 W m^{-2}), when the near-ice ocean temperature is above freezing and coincide with sea-ice basal melt.

We now focus on the high frequencies observed in the under-ice ocean data (SIMBA and SBE37). The daily resolution of the profiler data is not sufficient to examine the around 12 h period typical of tides and near-inertial internal gravity waves in the area.

4.1.2. High-Frequency Variations in Temperature and Salinity

The melting events, associated with ocean temperature peaks, also correspond to large high-frequency fluctuations detected in the 5 min sampling SBE37 data (Figure 8e). These high frequencies in salinity and temperature, retrieved when subtracting a 15 min running mean, have amplitudes up to 0.05 g/kg and 0.03°C and are largely anticorrelated ($r = -0.88$). These melt-associated high-frequency signatures could result from vertical mixing and overturning induced by salt releases from warming sea ice [*Widell et al*., 2006].

Variations with a close to 12 h period are conspicuous in certain parts of the SBE37 salinity time series (Figure 8f). They are less clear in the temperature time series because of the large temperature scale adapted to the large temperature range in Figure 8e. The close to 12 h period corresponds to the period of both semidiurnal tides and near-inertial internal waves generated in the upper ocean around 82°N, by passing storms or by geostrophic adjustment of strong mesoscale structures [*Dosser et al*., 2014]. Temperature and salinity variations in the 8–16 h bandwidth were extracted from the SBE37 data (Figure 8f). Salinity fluctuation amplitudes are below 0.006 g/kg most of the time except during the large melt events after 19 February where amplitudes larger than 0.05 g/kg are observed. Temperature fluctuations in this period range exceed 0.01°C for each melt event and even 0.35°C for the last event. This amplitude of 0.35°C corresponds approximately to an isotherm displacement of 15 m according to the last temperature profile (20 February 18:00: −1.15°C at 6 m and −0.70°C at 14 m).

In conclusion, the basal melt events until 21 February are associated with warming of the entire mixed layer when heat comes from the AW of the Svalbard Branch to the surface. Possible processes for the heat transfer from AW to the surface are discussed in section 4.2.

As observed in Fig. 3, basal melt is very active after February 21, when the only available data are that from SIMBA. SIMBA sensors do not have the accuracy of a SBE37 sensor and the sampling frequency was 3 h instead of 5 min. We cannot examine very high frequencies with the SIMBA data, however, we now show that we can get reliable information about the close to 12 h fluctuations. We produced three temperature time series out of the SIMBA profiles: two time series of the temperature averaged over 10 sensors around 3 and 4 m depth, and one time series of the temperature averaged over 75 sensors between 3 and 4.5 m. We applied an 8–16 h band-pass filter to the three temperature time series (Figure 8g). The three times series provide near 12 h fluctuations that are consistent with those extracted from the SBE37 data although with somewhat reduced amplitudes: variations near the 12 h period are observed during the melting events on 13, 16, and 20 February with similar amplitudes to those derived from the SBE37 during the first two small events and smaller amplitude on 20 February (Figure 8g). We now examine the full SIMBA time series.

4.2. Basal Ice-Melt Documented by SIMBA Data Until 15 March

Sea-ice melt is observed from 15 February to 2 March over the warm mixed layer of the Svalbard continental slope and estimated ocean to ice flux has a mean value of 100 W m^{-2} over those 2 weeks (Figures 9a

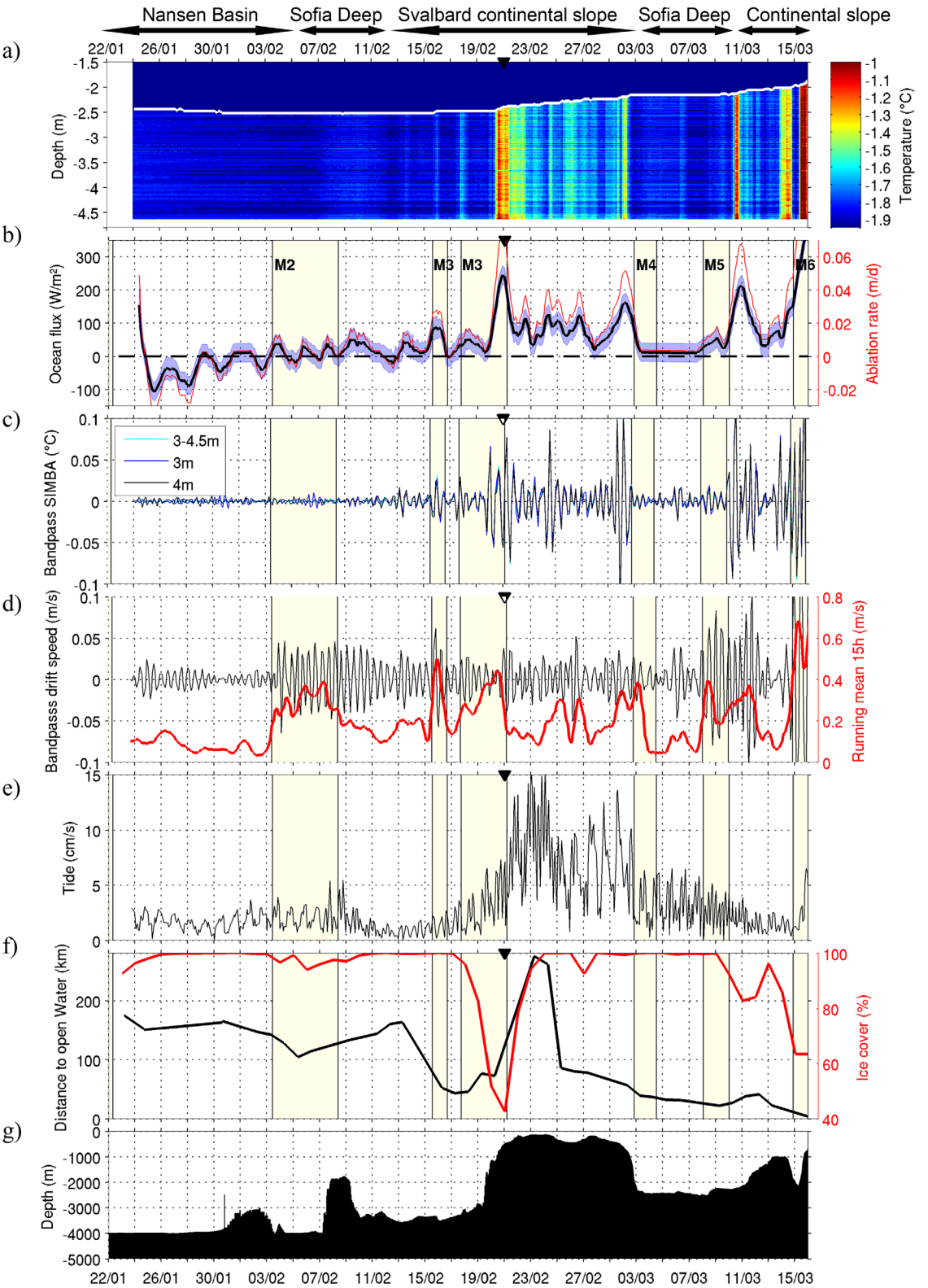

Figure 9. (a) SIMBA temperature zoomed on ocean from 22 January to 16 March. (b) Ocean flux (left axis, W m^{-2}) and ablation rate (right axis, m/d), at the ice/ocean interface deduced from the SIMBA data. Blue shaded area is the ocean heat flux uncertainty [*Provost et al.*, 2016]. The black triangle is the date after which there are no profiler data. (c) SIMBA temperature band-pass filtered between 8 and 16 h at 3 m (red), 4 m (blue) and averaged between 3 and 4.5 m (black). (d) Drift speed of IAOOS7 platform band-pass filtered between 8 and 16 h (left axis) and filtered using a 15 h running mean (right axis). (e) Tide velocity (m/s) from the AOTIM5 model [*Padman and Erofeeva*, 2004] colocated with the IAOOS7 platform drift. (f) Distance of SIMBA-2015h to open water (left axis) from *Itkin et al.* [2016] and colocated ice cover (%) from AMSR-2 (right axis). (g) Bathymetry along the track. Storm periods are shaded in light yellow.

and 9b). On 3 March, SIMBA drifts away from the continental slope (Figures 1 and 9d) and sea-ice melt stops as the under-ice water is at freezing temperature (−1.8°C, Figure 9a). Sea-ice melt resumes on 11 March, as the platforms drifts back over the continental slope and the shallow Svalbard Branch. A maximum sea-ice melt is observed at the end of the time series (15 March) as the platforms drifts southward over warm waters (around −1°C). The estimated heat flux then exceeds 350 W m^{-2} (Figure 9b). In 1 month, the SIMBA witnessed 71 cm of sea-ice basal melt.

In the SIMBA under-ice temperatures, large fluctuations with periodicities around 12 h and amplitudes reaching 0.1°C are observed and coincide with basal sea-ice melt (19 February to 2 March and 10–16 March) (Figures 9c and 9a). These large 12 h period fluctuations occur over rough topography (Figure 9g) and/or after large storms M5 and M6 (Figure 9c).

A variety of energy sources can generate near-inertial internal gravity waves with fluctuations close to 12 h, including atmospheric forcing [*Fer*, 2014], tides interacting over topography and geostrophic adjustment of mesoscale features [*Alford et al*., 2016]. Amplitudes of near-surface temperature variations at the near-inertial wave frequency estimated from the SIMBA observations (Figure 9c) were compared to ice drift speeds (Figure 9d), barotropic tide velocity amplitudes (estimated using AOTIM-5 model outputs, *Padman and Erofeeva* [2004] as in Meyer et al., (submitted manuscript)) (Figure 9e), sea-ice concentration from AMSR2 (https://earthdata.nasa.gov), distance to ice edge (P. Itkin et al., Sea ice deformation from the buoy array: Identification of deformation events and comparison to other datasets (SEDNA, FRAMZY, atmosphere), submitted to *Journal of Geophysical Research*, 2016, Figure 9f), and seafloor roughness (Figure 9g) to get some insight into the mechanisms responsible for those 12 h near-surface temperature variations. Ice drift speed was decomposed into inertial ice speed using the same 8-16 h band pass filter and subinertial low frequency ice speed (Figure 9d). Large amplitudes in inertial ice drift velocities are observed during and just after M3, and the ice pack concentration falls to 40% (Figures 9d and 9f). The presence of leads and open water (lower ice concentration) and the proximity to the ice edge (Figure 9f) allow more direct transfer of energy from the atmosphere to the ocean, as observed during the second part of M3 and during M5 and M6 (Figure 9c). The fluctuations in temperature with amplitude larger than 0.1°C could be storm-induced inertial waves. They are generated over ice-free ocean and detected when the platform is near open waters (ice edge or leads). The 12 h fluctuation signature in under-ice temperature is modulated by the depth of the thermocline: when the thermocline is below the pycnocline as in the Nansen Basin there is no signature of inertial waves in under-ice temperature.

The large episodic 12 h temperature fluctuations from 21 February to 3 March are concomitant with large tides over shallow topography at a time when the ice edge is distant by over 200 km and sea-ice concentration is close to 100%. The barotropic tide interacting with the shallow bottom topography could induce near-inertial waves with the observed under-ice temperature signal. As described in *Rippeth et al*. [2015], large bathymetry gradients associated with large barotropic tides can cause enhanced vertical heat flux from the AW across the pynocline through near-inertial waves development.

Geostrophic adjustment of mesoscale features can also generate near-inertial waves [*Alford et al*., 2016]. The largest 12 h under-ice temperature signal is observed over the maximum of gradient of the continental shelf (21 February, 3, 11, and 15 March, Figures 9g and 10), which corresponds with the offshore boundary of the Svalbard Branch (Figure 1).

The precise mechanisms that could have generated the near-inertial waves in the area are difficult to assess as tides, rough topography, and fronts are often concomitant when near-inertial wave signatures are recorded in the SIMBA and SBE37 data. Furthermore an internal wavefield is composed of both locally and remotely generated waves. The data do not permit to distinguish between locally generated downward propagating waves and remotely generated upward propagating waves. However, it seems that the wind has a major influence at the end of the time series when the platforms are in less compact ice, near leads or the ice edge, and that the tidal effects dominate from 10 February to 3 March.

5. Summary and Discussion

The deployment of IAOOS platforms during the N-ICE2015 campaign [*Granskog et al*., 2016] provided new insights on winter conditions in an area historically poorly sampled during that season (Meyer et al., submitted manuscript).

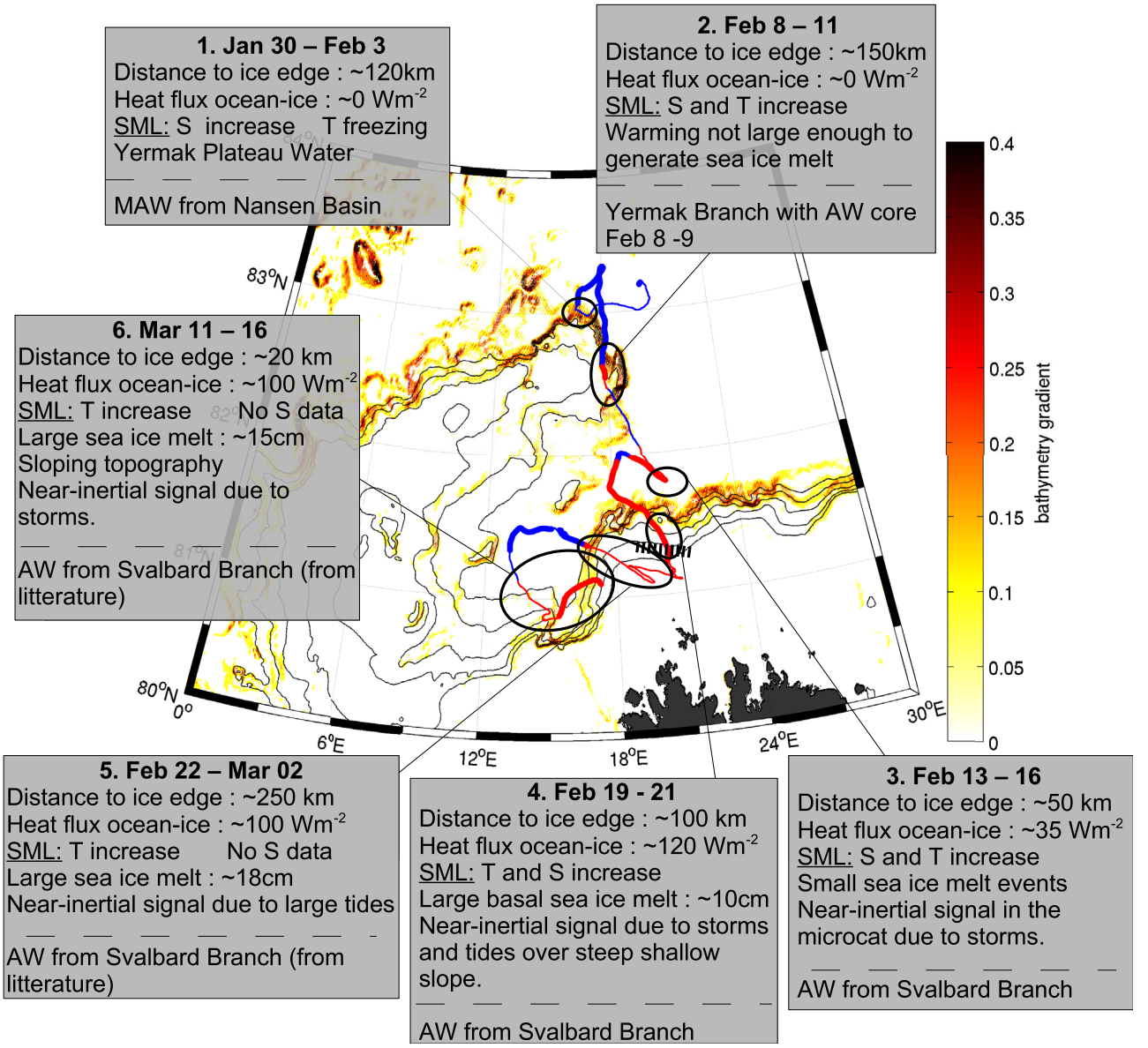

Figure 10. Summary of the study. Background is the bathymetry gradient amplitude (without units). Black contours are 0, 500, 700, 1000, 1500, and 2000 m depths. The drift trajectory is red when Floe 1 drifted over Atlantic Waters, and blue when Floe 1 drifted over the Modified Atlantic Waters. The trajectory is thick during storms and thin otherwise. The black dashed line (around 81.2°N, 20°E) in the map indicates the location of Floe 1 breakup when R/V Lance left and IAOOS7 continued drifting alone. The gray plots describe the ice-ocean interface and the warm water layer at several key locations. The dashed line in the panel separate comments on the surface (top part) and on the deep warm waters (bottom part).

The three regions crossed by Floe 1, the Nansen Basin, the Sofia Deep, and the Svalbard continental slope (Figures 7 and 10) presented distinct hydrographic conditions and ice-ocean interactions.

1. In the Nansen Basin the warm layer was deep, quiescent with layering in agreement with a description by *Rudels et al.* [2000] and capped by a stepped halocline due to local ice formation after summer melt as described in *Kikuchi et al.* [2004]. Ice was forming in the Nansen Basin as SIMBA-derived ocean-to-ice fluxes were negative and the upper layer salinity was larger than previously observed by 0.1 g/kg. A possible explanation for this larger salinity is that, in an Arctic region with thinner ice and leads, new-ice would grow faster in winter and salt release would be more important [*Ivanov et al.*, 2016].
2. Over the Svalbard continental slope, the warm AW from the Svalbard Branch was only 20–40 m from the sea surface. Profiler observations documented an ~70 km AW extension offshore the 500 m isobath and an offshore deepening of the AW over the continental slope. They were supportive of offshore AW eddy

shedding as recently documented further east (30°E) with velocity observations by *Våge et al*. [2016]. The lateral extension and mesoscale activity may be only winter features as the Atlantic Water inflow is seasonally variable with a larger transport in winter [*Hattermann et al*., 2016] (Z. Koenig et al., Atlantic Waters inflow north of Svalbard: insights from IAOOS observations and Mercator Ocean global operational system during N-ICE2015, submitted to *Journal of Geophysical Research*, 2016). SIMBA documented very large ocean surface temperature on the shelf and large sea-ice basal melt. Mixed layer temperatures were large because of enhanced local vertical heat fluxes from AW possibly due to: tides, mesoscale features, vertical convection during overturning events, steep bathymetry, or wind forcing near the ice edge and over leads.

3. In the Sofia Deep, the range of warm water characteristics was large and suggested different processes and water paths (Figures 7 and 10): upwelling of deep fresher water into the AW layer as possibly linked to tidal activity over rough topography [*Luneva et al*., 2015], mesoscale structures with AW cores from the Yermak Branch, the Svalbard Branch, or coming from the Yermak Pass (a passage through the Yermak Plateau deeper than 700 m at 81°N) [*Gascard et al*., 1995; *Rudels et al*., 2000] (Figure 7). High-resolution operational model outputs analyzed in a companion paper (Koenig et al., submitted manuscript) support these interpretations in terms of warm water paths and eddy activity.

The mixed layer was at the freezing temperature except above the Yermak Plateau slope and above the Svalbard Branch (Figure 10). The salty surface mixed layer located on the deep edge of the Yermak Plateau probably originates from the Yermak Plateau (Meyer et al., submitted manuscript). Operational model outputs confirm the difference in salinity between the salty Yermak Plateau and the fresh Nansen Basin mixed layers in winter (Koenig et al., submitted manuscript). The under-ice temperature, slightly above freezing over the deep slope of the Yermak Plateau, did not generate significant melt. In contrast, the thin and warm mixed layer above the Svalbard continental slope resulted in significant sea-ice melt in the middle of winter (Figure 10). The warming of the under-ice ocean is clearly visible in the SIMBA data. Near-inertial fluctuations in the under-ice temperature records suggest that near-inertial gravity waves bring heat from the shallow AW inflow up to the surface. However, the deep expression of the near-inertial signal could not be examined with the 12 h sampling of the IAOOS profiler during N-ICE2015. A higher sampling rate should be used in the future to enable studies like those by *Dosser et al*. [2014] or *Dosser and Rainville* [2016]. Near-inertial waves in the upper ocean formed over the Svalbard Branch could be caused by several mechanisms: tides interacting with topography, storms and mesoscale features. The largest near-inertial signal was observed close to the ice edge (Figure 10), in less packed ice, as the wind could directly force the ocean. In the changing Arctic, with more ice-free area and leads [*Willmes and Heinemann*, 2016], an increase in near-inertial waves is expected [*Dosser and Rainville*, 2016] potentially bringing heat up to the surface and promoting sea-ice melt.

In situ observations of large sea-ice basal melt (more than 71 cm in less than 2 months) over the Svalbard continental slope caused by heat coming from the Atlantic Water confirmed previous influences from theoretical considerations and indirect data [e.g., *Rudels et al*., 1996; *Ivanov et al*., 2016]. Large ocean-to-ice heat flux is a main process responsible for the sea-ice melt in winter north of Svalbard.

We showed that the easy-to-deploy SIMBA instrument can capture some near-inertial signals in the under-ice ocean temperatures. The deployment of a SIMBA network in the Arctic with a high-frequency sampling combined with current data would improve the monitoring of the near-inertial wavefield at a time when the Arctic is rapidly changing.

Acknowledgments
We thank Michel Calzas, Christine Drezen, Magali Garracio, Antoine Guillot, Jean-Luc Maria, Vincent Mariage, Jacques Pelon, and Jean-Philippe Savy for their contribution to the IAOOS platform preparation and tests. We also thank Ilker Fer, Mats Granskog, and Arild Sundfjord for their most valuable comments on the manuscript. This work was supported by the Equipex IAOOS (Ice Atmosphere Ocean Observing System) (ANR-10-EQPX-32-01), and by funding from the ICE-ARC program from the European Union 7th Framework Progamme grant number 603887. Z. Koenig acknowledges a PhD scholarship from Université Pierre et Marie Curie (UPMC). This work has been supported by the Norwegian Polar Institute's Centre for Ice, Climate and Ecosystems (ICE) through the N-ICE project. N-ICE acknowledges the in-kind contributions provided by other national and international projects and participating institutions, through personnel, equipment, and other support. The IAOOS platforms data are available at LOCEAN (Christine Provost, cp@locean-ipsl.upmc.fr).

References

Aagaard, K., A. Foldvik, and S. R. Hillman (1987), The West Spitsbergen Current: Disposition and water mass transformation. *J. Geophys. Res.*, *92*(C4), 3778–3784.

Alford, M. H., J. A. MacKinnon, H. L. Simmons, and J. D. Nash (2016), Near-inertial internal gravity waves in the ocean, *Ann. Rev. Mar. Sci.*, *8*, 95–123, doi:10.1146/annurev-marine 010814-015746.

Cokelet, E. D., N. Tervalon, and J. G. Bellingham (2008), Hydrography of the West Spitsbergen Current, Svalbard Branch: Autumn 2001, *J. Geophys. Res.*, *113*, C01006, doi:10.1029/2007JC004150.

Comiso, J. C. (2012), Large decadal decline of the Arctic multiyear ice cover, *J. Clim.*, *25*(4), 1176–1193, doi:10.1175/JCLI-D-11-00113.1

Dosser, H. V., and L. Rainville (2016), Dynamics of the changing near-inertial internal wave field in the Arctic Ocean, *J. Phys. Oceanogr.*, *46*, 395–415, doi:10.1175/JPO-D-15-0056.1.

Dosser, H. V., L. Rainville, and J. M. Toole (2014), Near inertial internal wave field in the Canada Basin from ice-tethered profilers, *J. Phys. Oceanogr.*, *44*, 413–426, doi:10.1175/JPO-D-13-0117.1.

Fer, I. (2009), Weak vertical diffusion allows maintenance of cold halocline in the central Arctic, *Atmos. Oceanic Sci. Lett.*, *2*(3), 148–152.
Fer, I. (2014), Near-inertial mixing in the central Arctic Ocean. *J. Phys. Oceanogr.*, *44*(8), 2031–2049, doi:10.1175/JPO-D-13-0133.1.
Gascard, J.-C., C. Richez, and C. Rouault (1995), New insights on large-scale oceanography in Fram Strait: The West Spitsbergen Current, in *Arctic Oceanography, Marginal Ice Zones and Continental Shelves*, vol. 49, edited by W. O. Smith, Jr. and J. M. Greibmeier, pp. 131–182, AGU, Washington, D. C.
Gill, A. E. (1982), *Atmosphere-Ocean Dynamics*, vol. 30, Academic, N. Y.
Granskog, M. A., P. Assmy, S. Gerland, G. Spreen, H. Steen, and L. H. Smedsrud (2016), Arctic research on thin ice: Consequences of Arctic sea ice loss, *Eos*, *97*, 22–26, doi:10.1029/2016EO044097.9.
Hattermann, T., P. E. Isachsen, W.-J. von Appen, J. Albretsen, and A. Sundfjord (2016), Eddy-driven recirculation of Atlantic Water in Fram Strait, *Geophys. Res. Lett.*, *43*, 3406–3414, doi:10.1002/2016GL068323.
Hudson, S., and L. Cohen (2015), *N-ICE2015 Surface Meteorology v1*. Norwegian Pol. Inst., Tromsø, Norway. [Available at https://data.npolar.no/dataset/056a61d1-d089-483a-a256-081de4f3308d.]
Ivanov, V. V., V. A. Alexeev, I. A. Repina, N. V. Koldunov, and A. V. Smirnov (2012), Tracing Atlantic Water signature in the Arctic sea ice cover east of Svalbard, *Adv. Meteorol.*, *2012*, 201818, doi:10.1155/2012/201818.
Ivanov, V., V. Alexeev, N. Koldunov, I. Repina, A. Sandø, L. Smedsrud, and A. Smirnov (2016), Arctic Ocean heat impact on regional ice decay—A suggested positive feedback, *J. Phys. Oceanogr.*, *46*, 1437–1456, doi:10.1175/JPO-D-15-0144.1.
Jackson, K., J. Wilkinson, T. Maksym, D. Meldrum, J. Beckers, C. Haas, and D. Mackenzie (2013), A novel and low-coast sea ice mass balance buoy, *J. Atmos. Oceanic Technol.*, *30*, 2676–2688, doi:10.1175/JTECH-D-13-00058.1.
Kikuchi, T., K. Hatakeyama, and J. H. Morison (2004), Distribution of convective Lower Halocline Water in the eastern Arctic Ocean, *J. Geophys. Res.*, *109*, C12030, doi:10.1029/2003JC002223.
Kikuchi, T., J. Inoue, and D. Langevin (2007), Argo-type profiling float observations under the Arctic multiyear ice, *Deep Sea Res., Part I*, *54*(9), 1675–1686.
Krishfield, R., J. Toole, A. Proshutinsky, and M. L. Timmermans (2008), Automated ice-tethered profilers for seawater observations under pack ice in all seasons, *J. Atmos. Oceanic Technol.*, *25*(11), 2091–2105, doi:10.1175/2008JTECHO587.1.
Luneva, M. V., Y. Aksenov, J.D. Harle, and J. T. Holt (2015), The effects of tides on the water mass mixing and sea ice in the Arctic Ocean, *J. Geophys. Res.*, *120*, 6669–6699, doi:10.1002/2014JC01310.
Manley, T. O. (1995), Branching of Atlantic Water within the Greenland-Spitsbergen passage: An estimate of recirculation, *J. Geophys. Res.*, *100*(C10), 20,627–20,634.
Manley, T. O., R. H. Bourke, and K. L. Hunkins (1992), Near-surface circulation over the Yermak Plateau in northern Fram Strait, *J. Mar. Syst.*, *3*(1), 107–125.
Mariage, V. (2015), *Développement et mise en œuvre de LiDAR embarqués sur bouées dérivantes pour l'étude des propriétés des aérosols et des nuages en Arctique et des forçages radiatifs induits*, UPMC, Villeurbanne, France. [Available at https://hal-insu.archives-ouvertes.fr/tel-01264610.]
Mariage, V., et al. (2016), IAOOS microlidar-on-buoy development and first atmospheric observations obtained during 2014 and 2015 arctic drifts, *Opt. Express.*, *119*, 4 pp.
McDougall, T. J., D. R. Jackett, F. J. Millero, R. Pawlowicz, and P. M. Barker (2012), A global algorithm for estimating Absolute Salinity, *Ocean Sci.*, *8*, 1123–1134.
Mc Phee, M. G., T. Kikuchi, J. H. Morison, and T. P. Stanton (2003), Ocean-to-ice flux at the North Pole environmental Observatory, *Geophys. Res. Lett.*, *30*(24), 2274, doi:10.1029/2003GL018580.
Muench, R. D., M. G. McPhee, C. A. Paulson, and J. H. Morison (1992), Winter oceanographic conditions in the Fram Strait-Yermak Plateau region, *J. Geophys. Res.*, *97*(C3), 3469–3483.
Onarheim, I. H., L. H. Smedsrud, R. B. Ingvaldsen, and F. Nilsen (2014), Loss of sea ice during winter north of Svalbard, *Tellus, Ser. A*, *66*, 23933, doi:10.3402/tellusa.v66.23933.
Padman, L., and S. Erofeeva (2004), A barotropic inverse tidal model for the Arctic Ocean, *Geophys. Res. Lett.*, *31*, L02303, doi:10.1029/2003GL019003.
Provost, C., et al. (2015), IAOOS (Ice-Atmosphere-Arctic Ocean Observing System, 2011–2019), *Mercator Ocean Quart. Newsl.*, *51*, 13–15. [Available at http://www.mercator-ocean.fr/eng/actualitesagenda/newsletter/newsletter-Newsletter-51-Special-Issue-with-ICE-ARC.]
Quadfasel, D., J. C. Gascard, and K. P. Koltermann (1987), Large scale oceanography in Fram Strait during the 1984 Marginal Ice-Zone Experiment. *J. Geophys. Res.*, *92*(C7), 6719–6728.
Rippeth, T. P., B. J. Lincoln, Y. D. Lenn, J. M. Green, A. Sundfjord, and S. Bacon (2015), Tide-mediated warming of Arctic halocline by Atlantic heat fluxes over rough topography, *Nat. Geosci.*, *8*(3), 191–194, doi:10.1038/ngeo2350.
Rudels, B. (2016), Arctic Ocean Stability: The effects of local cooling, oceanic heat transport, freshwater input and sea ice melt with special emphasis on the Nansen Basin, *J. Geophys. Res.Oceans*, *121*, 4450–4473, doi:10.1002/2015JC011045.
Rudels, B., L. G. Anderson, and E. P. Jones (1996), Formation and evolution of the surface mixed layer and the halocline of the Arctic Ocean, *J. Geophys. Res.*, *101*(C4), 8807–8821.
Rudels, B., R. Meyer, E. Fahrbach, V. V. Ivanov, S. Østerhus, D. Quadfasel, U. Schauer, V. Tverberg, and R. A. Woodgate (2000), Water mass distribution in Fram Strait and over the Yermak Plateau in summer 1997, *Ann. Geophys.*, *18*(6), 687–705.
Rudels, B., M. Korhonen, U. Schauer, S. Pisarev, B. Rabe, and A. Wisotzki (2015), Circulation and transformation of Atlantic water in the Eurasian Basin and the contribution of Fram Strait inflow branch to the Arctic Ocean heat budget, *Prog. Oceanogr.*, *132*, 128–152, doi:10.1016/j.pocean.2014.04.003.
Schauer, U., A. Beszczynska-Möller, W. Walczowski, E. Fahrbach, J. Piechura, and E. Hansen (2008), Variations of measured heat flow through the Fram Strait between 1997 and 2006, in *Arctic- Subarctic Ocean Fluxes: Defining the Role of the Northern Seas in Climate*, edited by R. R. Dickson, J. Meincke, and P. Rhines, pp. 65–85, Springer Sci, Amsterdam, Netherlands.
Sirevaag, A., and I. Fer (2009), Early spring oceanic heat fluxes and mixing observed from drift stations north of Svalbard, *J. Phys. Oceanogr.*, *39*(12), 3049–3069, doi:10.1175/2009JPO4172.1.
Sirevaag, A., S. D. L. Rosa, I. Fer, M. Nicolaus, M. Tjernström, and M. G. McPhee (2011), Mixing, heat fluxes and heat content evolution of the Arctic Ocean mixed layer, *Ocean Sci.*, *7*(3), 335–349, doi:10.5194/os-7-335-2011.
Steele, M., and J. Morison (1993), Hydrography and vertical fluxes of heat and salt northeast of Svalbard in Autumn, *J. Geophys. Res.*, *98*(C6), 10,013–10,024.
Timmermans, M. L., S. Cole. and J. Toole (2012), Horizontal density structure and restratification of the Arctic Ocean surface layer, *J. Phys. Oceanogr.*, *42*(4), 659–668.

Toole, J. M., M.-L. Timmermans, D. K. Perovich, R. A. Krishfield, A. Proshutinsky, and J. A. Richter-Menge (2010), Influences of the ocean surface mixed layer and thermohaline stratification on Arctic Sea ice in the central Canada Basin, *J. Geophys. Res.*, *115*, C10018, doi: 10.1029/2009JC005660.

Våge, K., R. S. Pickart, V. Pavlov, P. Lin, D. J. Torres, R. Ingvaldsen, A. Sundfjord, and A. Proshutinsky (2016), The Atlantic Water boundary current in the Nansen Basin: Transport and mechanisms of lateral exchange, *J. Geophys. Res. Oceans*, *121*, doi:10.1002/2016JC011715.

Widell, K., I. Fer, and P. M. Haugan (2006), Salt release from warming sea ice, *Geophys. Res. Lett.*, *33*, L12501, doi:10.1029/2006GL026262.

Willmes, S., and G. Heinemann, G. (2016), Sea-ice wintertime lead frequencies and regional characteristics in the Arctic, 2003–2015, *Remote Sens.*, *8*(1), 4, doi:10.3390/rs8010004.